Polymer 333 (2025) 128690

Contents lists available at ScienceDirect

Polymer

journal homepage: www.elsevier.com/locate/polymer

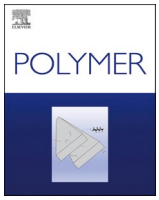

Ionic cluster driven polymer network formation: Macroscopic evidence of network reversibility by X-ray microtomography

Subhradeep Mandal [a,b], Arpita Kundu [a,b], Eric Euchler [a], Radek Stoček [c], Ricardo Bernhardt [a], Peter Reinig [h], Muhannad Al Aiti [d,i], Jun Sawada [e], Toshio Tada [e], Gianaurelio Cuniberti [d], Gert Heinrich [a,f], Sven Wießner [a,b], Amit Das [a,g,*]

[a] Leibniz Institute of Polymer Research Dresden, Dresden, 01069, Germany
[b] Institute of Materials Science, TUD Dresden University of Technology, Dresden, 01062, Germany
[c] Centre of Polymer Systems, Tomas Bata University in Zlín, Zlín, 760 01, Czech Republic
[d] Institute for Materials Science and Max Bergmann Center for Biomaterials, TUD Dresden University of Technology, Dresden, 01069, Germany
[e] Sumitomo Rubber Industries Ltd., Kobe, 6510072, Japan
[f] Institute of Textile Machinery and High-Performance Material Technology, TUD Dresden University of Technology, Dresden, 01069, Germany
[g] Tampere University of Applied Sciences, Tampere University, Tampere, 33720, Finland
[h] Fraunhofer Institute for Photonic Microsystems, Dresden, 01109, Germany
[i] Dresden Center for Nanoanalysis, Dresden, 01069, Germany

ARTICLE INFO

Keywords:
Reversible crosslinking
Ionic interaction
Cation-π interaction
X-ray microtomography
Tear-fatigue analysis
Cavity analysis

ABSTRACT

Significant progress has been made in the field of dynamic reversible networks in polymers, especially in unfilled systems. However, achieving similar reversibility in highly filled and mechanically robust elastomers with restricted chain mobility remains a formidable challenge. Furthermore, characterization techniques for assessing network reversibility are not significantly advanced beyond the traditional evaluation of mechanical properties before and after healing. To this end, a dynamic interaction was studied for bromobutyl rubber (BIIR) mixed with alkyl imidazole, which facilitates the formation of reversible ionic clusters within the elastomer matrix. Moreover, a special type of carbon black with graphitic microstructure was used as a filler not only to reinforce the elastomer, but also to form reversible bonds with the alkyl imidazolium ions by cation-π and π-π interactions. Through the synergistic effect of these interactions, the 1-butylimidazole-treated BIIR achieved excellent mechanical properties, including a tensile strength of 14 MPa and an elongation at break exceeding 1000 % with a self-healing efficiency of 71 %. X-ray microtomography studies provided compelling evidence of network reversibility in ionically treated BIIR. 3D reconstructions revealed that approximately 72 % of microcavities disappeared after healing, indicating enhanced material durability. The macro-scale durability was further assessed through tear-fatigue analysis, revealing significantly enhanced resistance to crack growth of the 1-butylimidazole-treated BIIR compared to its sulfur-cured counterpart. The formation of dual dynamic interaction in combination with advanced characterization techniques provides a comprehensive approach for the development of reversible materials and access to their reversibility for real-world scenarios.

1. Introduction

With the increasing focus on global sustainability, there is a growing demand for eco-friendly products made from biodegradable or recyclable materials. To address this societal demand, the development of a robust supply chain for recycled materials is the key solution. Nevertheless, a wide range of plastic materials can be recycled through either chemical or thermal recycling processes. In general, vulcanized rubber compounds are not suitable for recycling like plastics due to the presence of a permanent cross-linked network. However, one potential approach to addressing this issue involves the devulcanization and recycling of crosslinked rubbers by various means like thermo-mechanical [1], chemical [2,3], mechano-chemical [4,5], microwave [6], probe sonication [7], and so on. However, devulcanization of permanently sulfur-cured rubbers does not yet appear to be an effective solution due to the complicated devulcanizing procedures and

* Corresponding author. Leibniz Institute of Polymer Research Dresden, Dresden, 01069, Germany.
E-mail address: das@ipfdd.de (A. Das).

https://doi.org/10.1016/j.polymer.2025.128690
Received 21 March 2025; Received in revised form 10 June 2025; Accepted 14 June 2025
Available online 15 June 2025

deterioration of mechanical properties. Though devulcanization is all about selective scission of sulfur crosslinks, any recycling process of sulfur-cured rubber involves random scission and degradation of both polymer chains and crosslinks [3].

The introduction of sulfur-free reversible bonds into the rubber network is another effective strategy to enhance the re-processability of rubber products. Additionally, incorporating reversible bonds into the elastomer matrix to improve durability has become one of the most challenging and active areas of polymer research. Reversible bonds enable self-repair by continuously re-establishing cross-linking sites within the rubber network, thereby minimizing wear and tear during use [8,9]. To date, researchers have introduced many covalent and non-covalent interactions which can impart reversibility to elastomer networks. As far the dynamic covalent bond is concerned various mechanisms such as disulfide bonds [10], Diels-alder chemistry [11], Schiff base bonds [12], boronic ester crosslinking [13], trans-esterification and others have been established [14]. Integrating a dynamic non-covalent interaction is another approach which includes mechanisms like metal ligand interaction [15,16], hydrogen bonds [17,18], ionic interactions [19–21], zwitterionic network formation [22], van der Waals interaction and so on [23]. Despite the abundance of academic reports, these concepts have not yet been effectively implemented in real world applications. There are two primary reasons for this. First, most research focuses on gum rubber systems, where no reinforcing or functional filler particles are added. However, in real-world applications, the addition of conventional or nonconventional fillers is often necessary to enhance mechanical, thermal, and other viscoelastic properties [24,25]. In the gum system, the dynamics of polymer chains differ from those of filler-reinforced systems required for technical applications. The question arises as to whether these aforementioned molecular mechanisms remain still active in filler reinforced systems with restricted chain mobility. Moreover, the research on gum systems has demonstrated high self-healing efficiency at a very low level of mechanical properties only, which may suggest that the healing of the network is taking place due to chain diffusion in the partially cured pseudo-network structure [8]. The second problem lies in the inaccurate methodology to assess the reversible nature of the network structure in terms of accuracy and reproducibility. While conducting a self-healing experiment by bisecting the specimens and rejoining them under certain time-temperature conditions, many factors such as geometry and contact conditions between the two elastomer surfaces, surface inhomogeneity, stress concentration at the cutting edges due to notch effect, and so on may affect the efficiency of the healing process and the properties measured after healing [11,13,17]. Moreover, any prediction of material durability in real life conditions cannot be made using such a procedure.

This study focuses on the treatment of a commercially available elastomer, bromobutyl rubber (BIIR), with an alkyl imidazole. This treatment leads to the formation of imidazolium bromide groups, which can form ionic associates and thus influence the dynamics of the network structure. Furthermore, in order to achieve adequate mechanical properties, a special type of carbon black which has an exceptionally high surface area of 1000 m^2/g is added. The cation-π interaction between the imidazolium cation and the carbon black was expected to act as an additional mechanism for reversible crosslinking. Additionally, in this report, emphasis was put on establishing a more scientific method, rather than relying on traditional stress-strain measurements, to assess the healability of microscopic damages in the bulk. Currently, there is a dearth of research available on the fracture mechanical behavior of elastomeric materials under application oriented cyclic-dynamic conditions, which is the most essential characterization for the practical use of an elastomer material. Moreover, the initiation and propagation of sub-microscopic damages, such as cavitation, primarily stemming from failure events at nano and molecular scale, significantly influence macroscopic damage in the material. Crack growth measurements can thus provide direct evidence of the effectiveness of the dynamics of the network structure and offer insights into the service life extension of dynamically loaded rubber materials. The study presents a comprehensive analysis of tear fatigue behavior, specifically comparing the stable crack growth zone in crack growth vs tearing energy plot, for covalently cured and ionically treated BIIR. In addition, a thorough examination was conducted on rubber pancake samples characterizing the time dependent formation of microscopic damages, specifically cavities, in a controlled atmosphere in X-ray microtomography instrument. The objective is to observe the evolution and eventual disappearance of these cavities over time and compare it with covalently cured elastomer samples.

A comparison table summarizing relevant literature studies on BIIR rubber has been included as Supporting Information Table S1. The table highlights key differences in filler type, crosslinking method, mechanical properties, self-healing efficiency, and the characterization techniques employed to assess healing performance. This comparison demonstrates the distinct advantages of our approach in terms of both material design and evaluation methodology.

2. Materials and methods

Bromobutyl (BIIR) rubber (X_Butyl™ BB X2) was supplied by LANXESS AG, Germany. Carbon black (PRINTEX XE2B) was purchased from Orion Engineered Carbons (particle size <30 nm, surface area = 1000 m^2g^{-1}, Iodine adsorption number = 1125 mg g^{-1}, DBP adsorption number = 420 ml/100g). 1-butylimidazole was purchased from Sigma-Aldrich. Other materials such as zinc oxide (ZnO), magnesium oxide (MgO), Stearic acid, Sulfur and 2-mercaptobenzothiazole (MBT) were also purchased from Sigma-Aldrich and used without further purification.

The sample preparation is provided in the supporting information and an overview of the sample formulations is summarized in Table 1.

Tensile measurements of the dog bone shaped specimens were performed using Zwick 1456 tensile tester (ZwickRoell GmbH, Germany) according to DIN EN ISO 527-2/S2/200 at crosshead speed of 200 mm/min. Uniaxial cyclic tensile experiments were carried out for three cycles with different strains of 50 % (three cycles), 100 % (three cycles) and 200 % (three cycles) and then finally the samples were stretched up to failure.

The dynamic mechanical properties in strain sweep mode were investigated using EPLEXOR 2000 N (Gabo Qualimeter, NETZSCH-Gerätebau GmbH, Selb, Germany) at a constant frequency of 10 Hz at 20 °C. The dynamic strain range was set from 0.1 % to 30 % with a 60 % prestrain. For this experiment rectangular specimens ($35 \times 10 \times 2\ mm^3$) were used. The samples with the same size and geometry were also used for temperature sweep test in EPLEXOR 150 N (GABO QUALIMETER, NETZSCH-Gerätebau GmbH, Selb, Germany) at temperature range from −80 to 150 °C at a constant heating rate of 2 °C/min. The tests were conducted at 10 Hz frequency under dynamic strain of 0.5 % and static strain of 1 %.

The self-healing tests were performed using an in-house developed instrument with two brass blocks which can be joined together and separated. Firstly, standard dog bone shaped samples (DIN EN ISO 527-2/S2/200) with 2 mm thickness were punched and then placed in the instrument. Following this, the samples were cut at the middle with the

Table 1
Sample overview.

Abbreviation[a]	BIIR (g)	1-butylimidazole (phr)	Carbon black (phr)
BX10	100	0	10
BI4X10	100	4	10

[a] phr stands for parts per hundred rubber by weight. Another control compound is prepared with sulfur package consisting with 3 phr ZnO, 1 phr stearic acid, 1.5 phr MBT, 0.5 phr MgO and 0.5 phr sulfur. This sample is abbreviated as BSX10.

help of a sharp knife and then joined with a compression value of 0.1 mm. The instrument was then placed under different conditions (temperature and time) and mended samples were taken out for tensile measurements. The self-healing efficiency was calculated using the formula:

$$self-healing\ efficiency\ (\eta) = \frac{\varepsilon_{healed}}{\varepsilon_{pristine}} \times 100\% \quad (1)$$

Where ε is the elongation at break.

Scanning electron micrographs of the samples were conducted using a NEON 40 FIB-SEM workstation (Carl Zeiss Microscopy GmbH, Germany), operated under accelerating voltage (electron high tension, ETH) of 3.0 kV. Prior to acquiring the SEM images, the samples were sputter coated (Leica) with Platinum (thickness of 3.5 nm).

The microtomography studies were done using the device CT-ALPHA by ProCon X-Ray GmbH, Sarstedt, Germany. During the measurement, 120 kV of voltage and 200 μA of current were employed. The exposure time for each step was fixed at 773 ms. A complete rotation of the sample was performed with 1500 angles. A loading apparatus with a frame made of polycarbonate material was employed to fix and stretch the specimens [26]. The process of 3D data reconstruction was done using X-Aid software (Version 2022.12.3, MITOS GmbH, Munich, Germany) and the 3D analysis of cavities is conducted using the pore analysis module of VG Studio MAX software (Version 3.5.1., Volume Graphics GmbH, Heidelberg, Germany). The voxel resolution after reconstruction, uniform for all directions, was 12.2 μm.

To assess for the long-term durability of the rubbers, the material resistance against crack propagation was studied under dynamic loading conditions by monitoring fatigue crack growth (FCG) in plane strain samples. These samples were double-notched planar specimens with dimensions of 10 mm in length, 70 mm in width, and 1 mm in thickness [27]. The specimens were properly fixed by clamping bulges of 6 mm diameter via form-fitting. The FCG experiments were realized using a Tear and Fatigue Analyzer (TFA)®, Coesfeld GmbH & Co. KG, Germany. For all measurements, a Gaussian pulse with a pulse width of 10 Hz and a pulse repetition of 5 Hz was applied at room temperature. The FCG analysis was performed according to the experimental procedure introduced by Stoček et al. [27] In the first step, unnotched planar specimens were loaded under variation of the strain amplitude, ε, in the range of 3–35 %. For each of the six strain levels, 1500 loading cycles were applied. The average elastically stored energy, W_{el}, was estimated from the last ten cycles. The strain-depending tearing energy, T, was calculated considering the initial specimen length, l_0, by $T = W_{el}{}^{*}l_0$. Considering the results that express the material-dependent relationship between T and ε, the strain amplitudes for equivalent T values were estimated and defined for the FCG analysis on notched specimens. The initially 10 mm long notches were introduced by a razor blade perpendicular to the loading direction. Stable crack growth in rubber materials can be assumed under moderate loading conditions. At individual T levels, a fresh crack tip was produced by cutting again with a razor blade and a crack growth of ca. 1 mm was pre-defined for evaluating the crack growth rate, which is a relative value considering the change in crack length under a certain number of loading cycles (dc/dn).

Fatigue crack growth (FCG) analysis is a meticulously quantitative approach to evaluate the durability, and lifetime of elastomer composites [28].

Five distinct regions of crack growth can be observed in the crack growth vs tearing energy plot (Fig. 5a, Table 2). As long as the value of the tearing energy, T, is lower than T_0, the FCG proceeds at a constant rate, r, is very close to zero and it is solely attributable to ozone attack [29,30]. T_0 is a minimum energy required for the crack initiation of the fracture process. For a simple unfilled cross-linked rubber, this minimum energy primarily depends on the details of the polymer network, such as the average molecular weight between the cross-links, and on the weakest bond strength in the main polymer chain. It is, therefore, often called the intrinsic strength, T_0, as it only reflects the polymer chemistry as well as the network and practically represents the endurance limit of the rubber material. The mechanically caused FCG proceeds in a broad range of tearing energies between the intrinsic strength, T_0, and the critical ultimate strength, T_c. Within this range of T, a transient point at a tearing energy, T_{t0} is defined, which separates the range of tearing energies into two regions. At the region below T_t the dependence of the FCG rate, on the tearing energy, T, is linear in double logarithmic scale and above T_{t0} changes into a good approximation of the obtained data due to the power-law [$\frac{dc}{dn} = b{\cdot}T^m$], which defines the FCG region of stable crack growth. The end of the stable crack growth region then overcomes into a transient region, defined by the value of T_{tc}, in which the rate of crack growth accelerates to unstable growth. Finally, the crack proceeds to the unstable fatigue growth above the critical tearing energy, T_c, and the FCG rate becomes essentially infinite in the last region.

Table 2
Different regions in crack growth rate vs. tearing energy plot.

Region	Type of crack growth	General tearing energy validity region
1st	ozone-induced crack growth	$T < T_0$
2nd	transient crack growth to region of stable crack growth	$T_0 < T < T_{t0}$
3rd	stable crack growth	$T_{t0} < T < T_{tc}$
4th	transient crack growth to region of unstable growth	$T_{tc} < T < T_c$
5th	unstable crack growth	$T > T_c$

The values of intrinsic strength, T_0 can be measured directly by the TFA device, but it would take very long time and, therefore, to determine both intrinsic strengths, T_0 and ultimate strength, T_c values of the rubber compounds studied, an Intrinsic Strength Analyser (ISA, Coesfeld GmbH & Co. KG, Germany) is applied. The analysis is based on testing protocol developed by Endurica LLC (OH, USA) using the cutting method of Lake and Yeoh [31]. Standard ISA testing methodology consists of several steps and was thoroughly described in the paper [32].

Raman spectroscopy was performed using the confocal Raman microscope inVia Qontor, Renishaw plc. including a DM2700 microscope (Leica Camera AG) and 20 x 2 NPLAN-objective lenses with working distance of 1.15 mm. For excitation, a solid-state continuous wave laser (TEM00, polarization ratio 100:1, vertical) operating at wavelength (532.1 ± 0.3) nm with maximum output power of 50 mW has been employed. Sample illumination was performed with 0.5 mW laser power perpendicular to the sheet-like sample surface. Measurements were conducted in the Stokes-regime using a Rayleigh filter with 100 cm^{-1} cut-off wavenumbers. The spectral resolution of the system is < 1.0 cm^{-1} for the full width at half maximum (FWHM), with a long-term spectral stability in the range of ±0.05 cm^{-1}. Raman spectra acquisition was conducted at an exposure time of 10 s per individual spectrum and an integration of twelve subsequent individual measurements. After the acquisition of the raw spectra, a baseline correction was performed, and spectra were normalized to maximum intensity. Each sample was measured 12 times, and a mean curve was built based on the 12 measurements and the mean curve was then normalized in the range 0–1. The peak deconvolution and non-linear curve fitting were performed using OriginLab2019Pro. Gaussian-Lorentzian-Cross model was used to fit the peaks, and the utilized iteration algorithm was Levenberg-Marquardt. Confining the quality of the fitting was done by considering the fit to be converged when the Chi-square tolerance value of 10 and the corrected Pearson correlation coefficient of >0.99 were reached. The apparent bulk value of the estimated lattice size was calculated using the equation of Cançado et al. [33].

$$L_a = \left(2.4x10^{-10}\right)\lambda_l^4 (I_D/I_G)^{-1} \quad (2)$$

Where λ_l is the wavelength of the excitation laser, which is 532 nm; and L_a is the in-plane crystallite size.

3. Results and discussion

Fig. 1a shows the torque profile of different mixing processes of BIIR, XE2B carbon black and 1-butylimidazole. This figure shows that the presence of XE2B carbon black considerably increases the temperature of the mixing chamber of the internal mixer for BX10 and BI4X10. In the case of BX10, the final torque steadily decreases over time. However, in the case of BI4X10, an increase in torque is observed. The increasing torque could be attributed to the formation of imidazolium bromide ionic associates as well as the interaction between the cation and π cloud of XE2B. Moreover, rheometric curves obtained with the Rubber Process Analyzer (RPA) provide additional insight into the effect of temperature on the break-up and regeneration processes of the ionic clusters (Fig. 1b). At lower temperatures, specifically at 100 °C and 120 °C, the torques are higher and quite stable due to the formation of ionic associations, however, as the temperature increases, the torque reverses. The reversal can be attributed to the breaking of the ionic associations. It is worth noting that 1-butylimidazole does not offer any bi-dentate crosslinking sites for bromobutyl rubber. 1-butylimidazole can only react with the bromine, resulting in the formation of imidazolium bromide, where the imidazolium group attaches to the main polymer chain and the bromide ion remains as a free anion (Fig. 2a). This reaction, known as the Menshutkin reaction, converts a tertiary amine into a quaternary ammonium salt through its reaction with an alkyl halide [34, 35]. Since no other crosslinking agents are present, the increase in rheometric torque can only be attributed to the formation of ionic clusters and a network created through physical interactions with carbon black. In this context, the carbon black particles act as multifunctional crosslinking sites. To investigate the interaction between carbon black and the imidazolium-grafted rubber chains, Raman spectroscopy

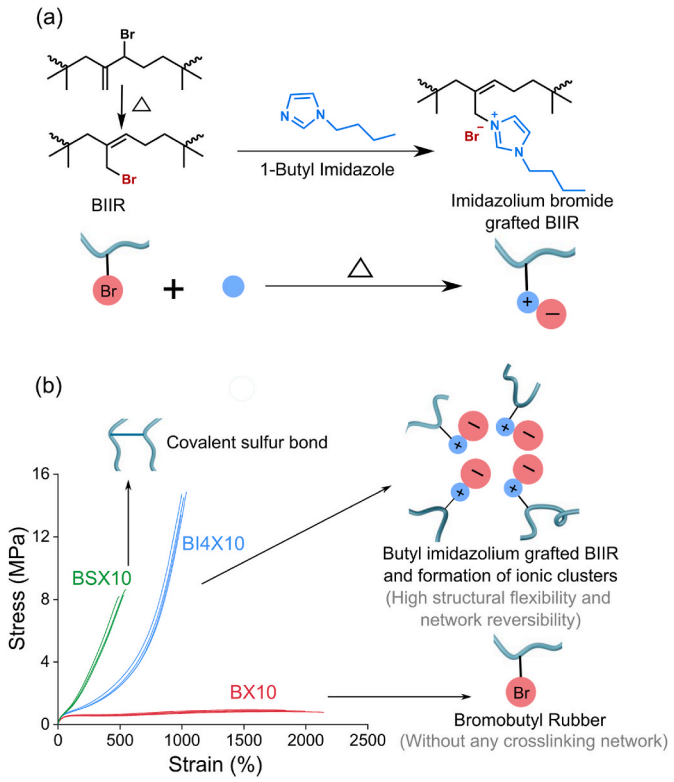

Fig. 2. (a) Grafting of 1-butylimidazole onto the bromobutyl rubber chain and formation butyl imidazolium bromide ion pairs, (b) stress-strain plots of carbon black filled uncrosslinked bromobutyl rubber (BIIR), carbon black filled sulfur-cured BIIR, and carbon black filled butyl imidazolium bromide ion grafted BIIR.

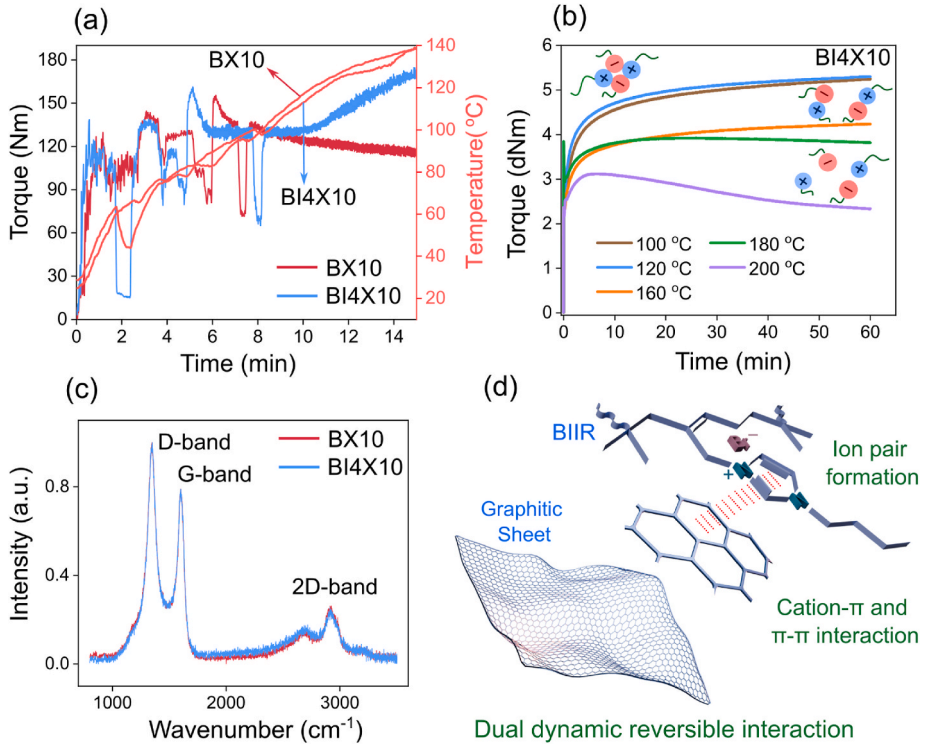

Fig. 1. (a) Plot of torque and temperature as a function of time for BX10 and BI4X10 composites in the mixing chamber during the mixing Process, (b) rheometric torque vs time plot of BI4X10 at different temperatures from 100 to 200 °C obtained from RPA, (c) comparative analysis of Raman Spectra for BX10 and BI4X10 composites, (d) schematic representation of dual dynamic reversible interactions in the elastomer matrix of BIIR: firstly, imidazolium bromide ion pair formation followed by cation-π and π-π interaction between the graphitic layer of XE2B and imidazolium cations.

was performed. Previous analyses using secondary ion mass spectroscopy (SIMS) and X-ray photoelectron spectroscopy (XPS) have demonstrated that XE2B carbon black possesses a high level of graphitic character on its surface [36]. The Raman spectra of the BI4X10 and BX10 are shown in Fig. 1c. The fitted curves are presented in the supporting information Figure S1. From the fitted curves the positions of the D-, G-, and 2D-band are summarized in Table 3. Also, the total fit area of the D-band and G-band was used to calculate the area intensity ratio of the D and G-band which contains also the information of the FWHM of both bands. Table 3 indicates that *in-situ* 1-butylimidazole modification of the elastomer reduces the area ratio of D- and G-band by 16.5 %. Furthermore, the values of the FWHM of the G-, and D-band did not significantly change, which assesses the fact that the carbon black maintained its structure under the two different conditions of processing (with and without 1-butylimidazole). The positions of the D- and G-band maintained the same values. Only the 2D-band showed a reduction by 42 cm^{-1} in the case, where 1-butylimidazole was added to the structure.

The bulk values of the in-plane crystallite size seem to be slightly decreased from 13.7 nm for the samples that are not treated with 1-butylimidazole to 12.8 nm for the samples that are treated with it. A possible explanation could be that the imidazolium cations preferably interact or adsorb via cation-π or π-π interactions to the surface of the turbostratic domains and slightly deformed the turbostratic structure during mixing (Fig. 1d).

The stress-strain plot demonstrates that grafting imidazolium cations in the BIIR backbone strikingly improved the mechanical properties of the composites (Fig. 2b). The tensile strength increased from 0.3 MPa in BX10 to 14 MPa in BIM4X10. Since the 1-butylimidazole based network structure cannot be involved with the unsaturation part of BIIR backbone, the mechanical properties can solely be attributed to the ionic clustering effect and cation- π interaction with the carbon black particles. Fig. 2a illustrates the grafting of 1-butylimidazole onto the BIIR backbone, along with the formation of ionic clusters of imidazolium bromide groups within the elastomer matrix. Now, as far as the sulfur-cured BIIR is concerned, it shows lower tensile strength as well as lower elongation at break as compared with 1-butylimidazole-treated BIIR (Fig. 3a). However, a crossover in the modulus value can be observed near 30 % strain (Fig. 3b).

Prior to this point, the sulfur-cured BIIR exhibits a lower modulus value compared to the 1-butylimidazole-treated BIIR. However, beyond this point, there is a sharp increase in the modulus. The stress value at 200 % strain for BIIR treated with 1-butylimidazole was 1.0 MPa, significantly lower than the stress value of 2.3 MPa for BIIR cured with sulfur. The higher modulus observed in sulfur-cured BIIR can be attributed to both the density and nature of the crosslinking within the material. The crossover can also be observed in the cyclic stress-strain plot (Fig. 3c and d). Here, up to 200 % strain, the 1-butylimidazole-treated BIIR demonstrated a lower area in the hysteresis loops than the sulfur-cured BIIR, indicating a higher elasticity in the network structure of the 1-butylimidazole-treated BIIR (Fig. 3c and d). The area under the first hysteresis loop at 200 % strain for BSX10 is 56 × 10^{-3} J, which is significantly higher than the 48 × 10^{-3} J observed for BI4X10 (Inset Fig. 3c).

Table 3
Raman parameters from the fitting procedure.

Sample	BX10	BI4X10
D-band (cm^{-1})	1346	1348
G-band (cm^{-1})	1604	1603
2D-band (cm^{-1})	2969	2927
FWHM D-band (cm^{-1})	88.7	89.1
FWHM G-band (cm^{-1})	59.9	59.3
I_D/I_G	1.4	1.5
Peak position (amorphous carbon)	1515	1529
Integral area (amorphous carbon) (a. u.)	29.5	28.5
A_D/A_G (−)	2.49	2.14
L_a* (nm)	13.7	12.8

It is important to note that swelling experiments were also conducted to estimate the crosslinking density of both sulfur-cured and butylimidazole-treated BIIR composites. While conventional swelling methods using toluene are effective for systems with covalent crosslinks, they may not be suitable for materials containing non-covalent, dynamic interactions such as ionic clusters. Nonetheless, a standard swelling test was performed. In this experiment, 0.5 g of each sample was immersed in 50 mL of toluene for 3 days assuming equilibrium is achieved. For the sulfur-cured BIIR, swelling occurred as expected, and we were able to calculate the swelling index. In contrast, the ionically modified BIIR gradually dissolved in toluene over the same period due to the non-covalent nature of the interactions, making it impossible to determine a measurable weight or swelling index (Supporting information Figure S2).

Fig. 4a and b presents the temperature sweep dynamic mechanical analysis (DMA) results for 1-butylimidazole-treated and sulfur-cured BIIR. In the plot of loss modulus against temperature both sulfur-cured and 1-butylimidazole-treated samples show a similar glass transition temperature which is around −50 °C. In the case of tan δ vs temperature curve, it is typically observed that both BIIR samples exhibit a broad asymmetric relaxation pattern with a prominent peak at lower temperatures (−44 °C) and a shoulder at higher temperatures (−23 °C). The tan δ peak at −23 °C is associated with the cooperative movement of the rubber chain segments or glass transition process (α process) where a relatively high number of chain segments is involved. Additionally, the shoulder peak of tan δ around −44 °C corresponds to the β process that arises from the local segmental motion, commonly known as the sub-Rouse modes. In this process very few (~10 backbone bonds) chains are involved [37]. Additionally, in Fig. 4b, a distinct broad peak well above the glass transition (high temperature peak) is observed near 90 °C for the 1-butylimidazole-treated BIIR, whereas this peak is not present in case of sulfur-cured BIIR. This broad peak can be attributed to the presence of ionic clusters and the interaction between the cations and π clouds of XE2B carbon black in the elastomer matrix [38,39].

Thermogravimetric Analysis (TGA) was performed for 3 composite formulations: pristine BIIR (without filler), BI4X10 (butyl imidazole-treated BIIR with XE2B), and BSX10 (sulfur-cured BIIR with XE2B). As shown in the TGA curve (supporting information Figure S3), all filled composites (BI4X10, BSX10) exhibit improved thermal stability compared to pristine BIIR. For instance, the temperature corresponding to 20 % weight loss increases from 335 °C in pristine BIIR to 358 °C, and 374 °C in BI4X10, and BSX10, respectively. This enhancement can be attributed to the presence of XE2B carbon black and the interactions with the polymer matrix. However, aside from this moderate improvement in degradation temperature, no additional significant difference was observed among the samples.

Dynamic mechanical strain sweep experiments are generally used to evaluate stress-induced re-agglomeration processes of fillers, known as "filler flocculation." The breakdown of filler aggregates and the increased energy dissipation during dynamic mechanical loading, known as the Payne effect, is compared for both the sulfur-cured and 1-butylimidazole-treated composites in Fig. 4c. In order to accurately investigate the dependence of storage modulus under dynamic strain amplitude, a phenomenological model proposed by Kraus is employed [40,41]. The corresponding equation can be expressed as:

$$E'_\gamma = \frac{E'_0 - E'_\infty}{1 + (\gamma/\gamma_c)^{2m}} + E'_\infty \quad (3)$$

where, E'_0 represents the storage modulus at a very low strain amplitude whereas E'_∞ denotes the storage modulus at a very high strain. E'_γ represents the storage modulus at a dynamic strain amplitude γ. γ_c represents the critical strain where the value of $E'_0 - E'_\infty$ approaches almost half of its original value. Furthermore, the shape of the storage modulus curve is represented by m. From Fig. 4c, it can be observed that the filler-

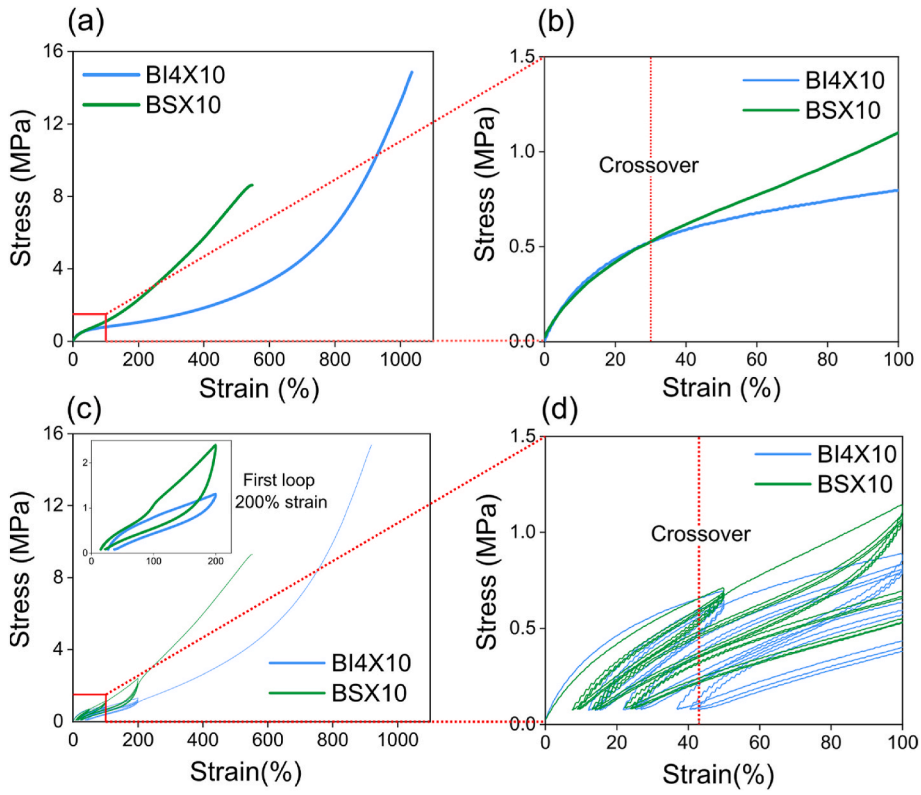

Fig. 3. (a) The stress-strain plots of 1-butylimidazole-treated and sulfur-cured BIIR, (b) cyclic uniaxial stress-strain plots of 1-butylimidazole-treated and sulfur-cured BIIR, (c, d) the cyclic uniaxial stress strain properties up to 200 % strain.

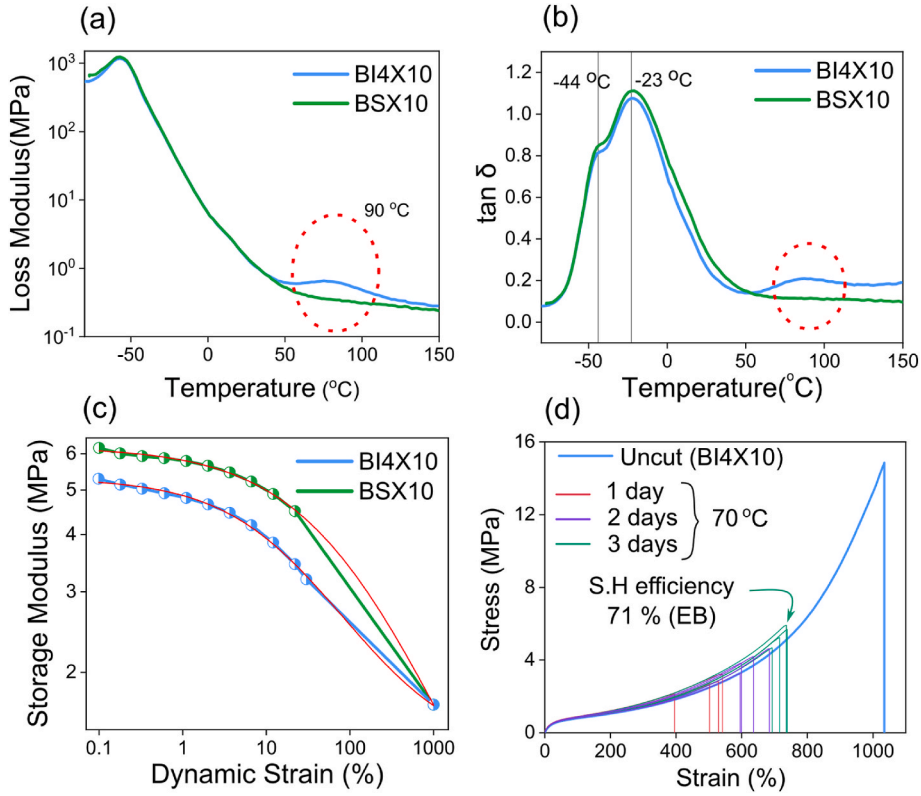

Fig. 4. Dynamic mechanical analysis, (a) loss modulus as a function of temperature and (b) tan δ vs temperature plot for 1-butylimidazole-treated and sulfur-cured BIIR; (c) Payne effect measurement for 1-butylimidazole-treated and sulfur-cured BIIR, Kraus equation is fitted in double logarithmic plot of storage modulus vs dynamic strain; (d) self-healing efficiency was calculated by comparing the mechanical properties of uncut specimens with those of mended specimens after conditioning at 70 °C for 1–3 days.

rubber interaction is much higher in the case of 1-butylimidazole-treated BIIR than compared to the sulfur-cured BIIR. Moreover, the critical strain value (γ_c) for 1-butylimidazole-treated BIIR is 114 which is significantly higher than the sulfur-cured BIIR with a critical strain value of 27. The higher critical strain value of 1-butylimidazole-treated BIIR can be attributed to the affinity of the carbon black towards imidazolium cation rich zones in the elastomer matrix through cation-π interaction. To investigate the macro-level effects of reversible interactions, self-healing tests were conducted on 1-butylimidazole-treated BIIR composites. Here the optimization of temperature for self-healing is crucial and strongly depends on the specific elastomeric system and the underlying reaction mechanism of regeneration and breaking of reversible bonds. In general, increasing the self-healing temperature can enhance molecular mobility and reaction rates, thereby promoting faster and more efficient healing. However, higher temperatures may also accelerate undesirable side reactions or even initiate thermal degradation of the polymer matrix, especially over prolonged duration. In this study, the effect of temperature on self-healing behavior was systematically investigated, identifying 70 °C as the optimal self-healing temperature. The tests were carried out over a duration of 1–3 days. Results indicated a gradual increase in self-healing efficiency with time, achieving a 71 % efficiency in terms of elongation at break after 3 days (Fig. 4d). SEM micrographs of the healed specimens, showing the cut line, are provided in supporting information Figure S4. It is noteworthy that higher self-healing efficiency is more attainable in unfilled elastomers, owing to the unrestricted mobility of rubber chains and the pseudo-crosslinking of the elastomer network [8]. However, in a filled elastomer matrix (containing 10 phr of carbon black with a surface area of 1000 m^2/g) with complete crosslinking (as evidenced by the plateau in rheometric torque in Fig. 1b) achieving a 71 % self-healing efficiency represents a significant accomplishment. Moreover, it is noteworthy that the CB used here is highly reinforcing in character with very high surface area of 1000 m^2/g. It is well established that high mechanical performance in BIIR systems, particularly a tensile strength of 14 MPa and an elongation at break of around 1000 % is closely linked to effective dispersion of the filler. SEM images further support this, revealing no significant agglomeration of carbon black, thereby indicating a reasonably uniform distribution within the BIIR matrix (Supporting information Figure S4).

Unlike conventional self-healing studies, fracture mechanical behavior under cyclic-dynamic conditions is a more scientific and quantitative technique for studying the network reversibility as well as extended lifetime of elastomer materials. In the present study, the stable crack growth regime is compared for the sulfur-cured and 1-butylimidazole-treated BIIR [19]. Fig. 5a represents a typical crack growth rate vs tearing energy plot. Fig. 5c demonstrates that 1-butylimidazole-treated BIIR exhibited significantly reduced crack growth rates compared to sulfur-cured BIIR. In the case of lower tearing energies, e.g. at $T < 100$ J/m^2, a crossover can be assumed, which is confirmed with the data presented in Fig. 5d in which the T_0 for sulfur-cured BIIR became larger as compared to 1-butylimidazole-treated BIIR. The lower crack growth rate in case of 1-butylimidazole-treated BIIR can be attributed to the dissociation and reassociation of the imidazolium bromide ionic aggregates. In the presence of ionic aggregates in the elastomer matrix, the dissociation of the ionic pairs takes place due to the stress concentration at the crack tip. Due to the dissociation of ionic pairs, the stress could be distributed in the matrix. Moreover, those dissociated ionic pairs can rearrange themselves with other ions in the vicinity by an ionic hopping mechanism which further resists the crack propagation (Fig. 5b). Additionally, Fig. 5d confirmed the lower critical tearing energy (T_c) for sulfur-cured BIIR compared to 1-butylimidazole-treated BIIR. This observation aligns with the trends in FCG slopes, where a higher slope (m) corresponds to a lower critical tearing energy (T_c) for sulfur-cured BIIR, and the reverse is true for 1-butylimidazole-treated BIIR.

The integration of self-healing characteristics is important because it is expected to significantly enhance the lifespan and durability of an elastomer. The molecular level mechanisms such as ionic interactions, reversible hydrogen bonding, and cation-π interactions may play a crucial role in inhibiting microcrack formation and facilitating the healing of microcracks in elastomeric materials. Thus, investigation of formation and transformation of (sub)-microscopic defects mainly originating from failure events at the nano- or molecular scale is crucial for understanding the reversibility or self-healability of the network structure in the elastomer matrix.

In the whole course of the experiment (Table 4) when the sample was undergoing X-ray scanning, simultaneously the stress relaxation in the samples was also recorded (Fig. S5 of the supporting information). It can

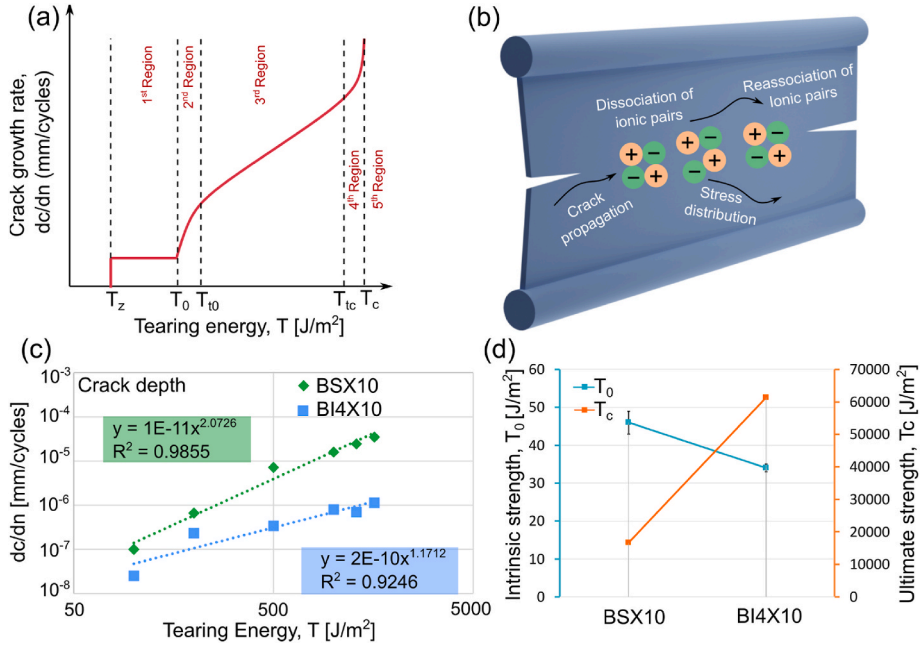

Fig. 5. (a) A plot showing different stages of fatigue crack growth rate as a function of tearing energy, (b) an illustration showing how dissociation and reassociation of ionic pairs leads to lower crack growth in an ionically treated elastomeric matrix; (c) fatigue-crack growth rate versus tearing energy plot and (d) intrinsic and ultimate strengths for sulfur-cured and 1-butylimidazole-treated BIIR.

Table 4
Different Stages of X-ray microtomography experiment.

Stages	Conditions
1	Without load
2	Load 100 N (BI4X10)
	Load 80 N (BSX10)[a]
3	Load removed (10 min)
4	Kept 3 days at room temp
5	Load 100 N (BI4X10)
	Load 80 N (BSX10)
6	Load removed (10 min)
7	Kept 3 months at room temp.
8	Load 10 N

[a] In the case of BSX10 only load up to 80 N could be achieved.

be observed that the initial stress decay for sulfur-cured BIIR is lower than the 1-butylimidazole-treated BIIR. Moreover, after the initial relaxation of BSX10, the relaxation force was maintained to a certain level approaching a plateau. Nevertheless, in the case of 1-butylimidazole-treated BIIR, a continuous stress decay was observed. It can be attributed to the ionic clustering effect in the 1-butylimidazole-treated BIIR matrix, where due to the mechanical loading the anchoring points of a rubber chain can slip from one cluster to another cluster and thus a continuous relaxation may be associated with this phenomenon. Figs. 6 and 7 compare the two- and three-dimensional images of cavities acquired from the X-ray microtomography experiment. In the initial two-dimensional images, the slice of the undamaged pancake specimen can be seen (Figs. 6a and 7a). However, formation of cavities started upon applying load. Sulfur-cured BIIR showed cavities all over the specimen, however, 1-butylimidazole-treated BIIR showed a comparatively lower number of cavities which are concentrated in the center of the specimen due to the higher stress concentration in the center (Figs. 6b and 7b). It is important to note that comparing two different types of rubbers with different network structures under the same load is challenging. This difficulty arises because the onset of cavity formation and their growth steps for two different composites depends on their distinct positions on two dissimilar load- displacement curves. Cyclic stress vs strain curves of pancake shaped specimens (10 mm radius and 1 mm thickness) of 1-butylimidazole-treated and sulfur-cured BIIR composites are presented in Fig. S6 of the supporting information. Based on the two-dimensional image of sulfur-cured BIIR, it can be inferred that poor carbon black dispersion within the elastomer matrix (as supported by the Payne effect measurement in Fig. 4c) leads to high local

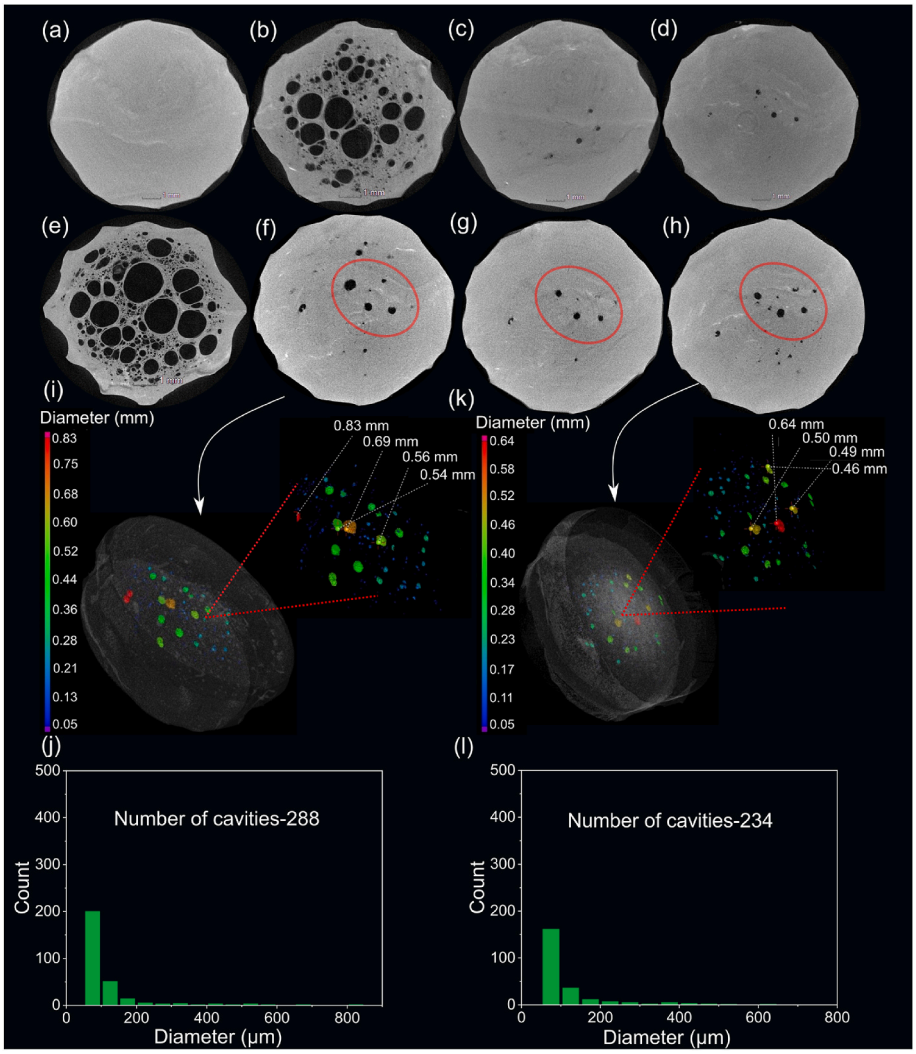

Fig. 6. A two-dimensional illustration with a representative slice for each case for sulfur-cured BIIR in different conditions, (a) initial image prior to the formation of cavities, (b) image obtained after application of 80 N load, (c) image after the load is removed, (d) image obtained after resting for 3 days in room temperature, (e) image acquired after the 80 N load applied for the second time, (f) image after removing load for the second time, (g) image after resting the sample for 3 months in room temperature, (h) image after applying 10 N load; three dimensional cavity analyses for (i), (j) the sample after removing the 80 N load for second time (corresponding to the two dimensional image f), and (k), (l) the final image after applying 10 N load (corresponding to the image h).

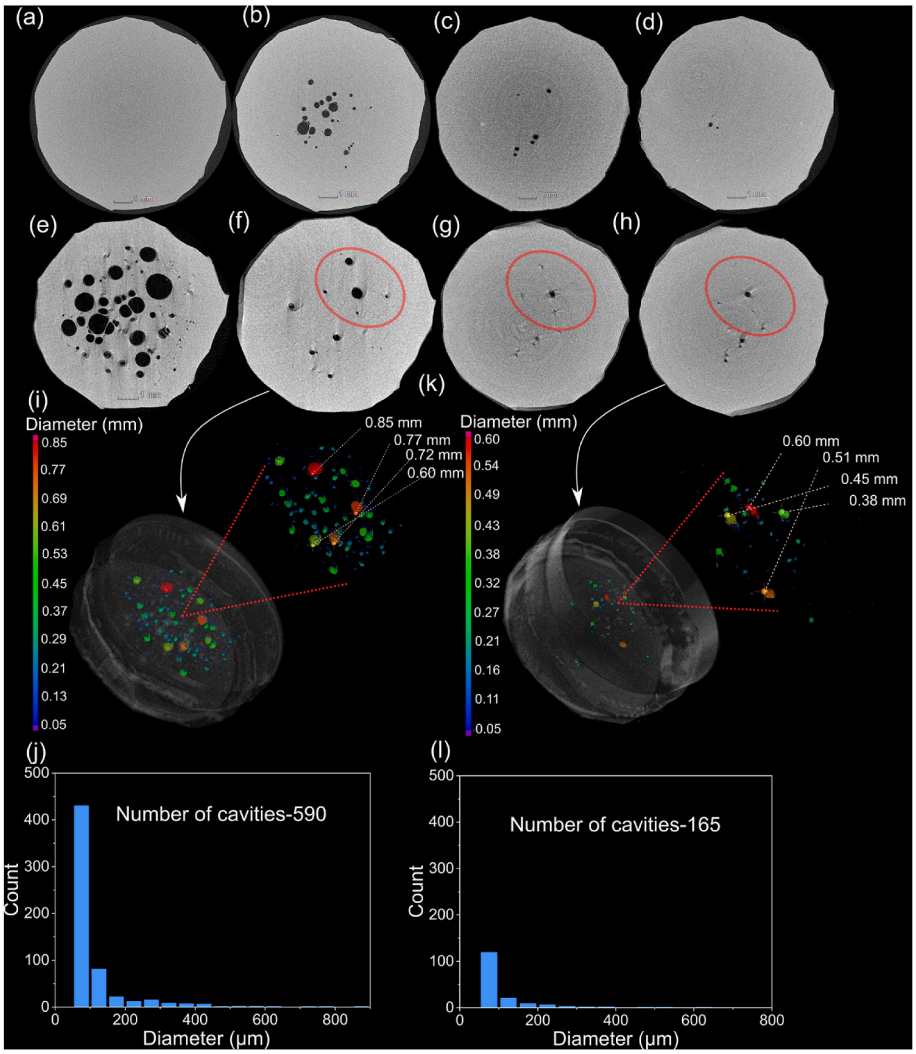

Fig. 7. A two-dimensional illustration with a representative slice for each case for 1-butylimidazole-treated BIIR in different conditions, (a) initial image prior to the formation of cavities, (b) image obtained after application of 100 N load, (c) image after the load is removed, (d) image obtained after resting for 3 days in room temperature, (e) image acquired after the 100 N load applied for the second time, (f) image after removing load for the second time, (g) image after resting the sample for 3 months in room temperature, (h) image after applying 10 N load; three dimensional cavity analyses for (i), (j) the sample after removing the 100 N load for second time (corresponding to the two dimensional image f), and (k), (l) the final image after applying 10 N load (corresponding to the image h).

stress concentrations caused by agglomerates, resulting in the development of multiple microcavities that subsequently coalesce into larger cavities. For 1-butylimidazole-treated BIIR, the effective carbon black dispersion, facilitated by cation-π interactions, ensures a strong rubber-filler interaction. Consequently, the reduced number of cavities could be attributed to microbubbles or pre-existing micro-defects, which then grow independently. In the third stage after the load is removed, a significant decrease in the cavity number and size could be observed in both of the cases (Figs. 6c and 7c). The fourth stage represents a healing phase (Figs. 6d and 7d). In the two-dimensional images of sulfur-cured BIIR, some cavities remain but differ from those in the previous stage. In 1-butylimidazole-treated BIIR, the healing stage shows a further reduction in the number of cavities. In the fifth stage, which represents the second loading phase, a significant increase in the number of cavities is observed in both sulfur-cured and 1-butylimidazole-treated BIIR (Figs. 6e and 7e). The previously formed irreversible cavities serve as additional nucleation points for the formation of new cavities, contributing to the overall increase in cavity numbers during this stage. In the sixth stage, which is one of the relaxation stages for both composites, a reduction in the number of cavities is observed (Figs. 6f and 7f). To accurately quantify the number and size of these cavities, a three-dimensional reconstruction of various sample slices was performed using VG Studio MAX software. This reconstruction allows for the observation of three-dimensional cavities (in sphere form) within the bulk of the pancake-specimen. Among all the cavities, four larger ones are highlighted in the image (Figs. 6i and 7i). The largest cavity diameters are comparable between the two composites, measuring 0.83 mm in sulfur-cured BIIR and 0.85 mm in 1-butylimidazole-treated BIIR. Nonetheless, the 1-butylimidazole-treated BIIR has a higher number of cavities, with a total of 590, compared to the sulfur-cured BIIR, which has a total of 288 existing cavities (Figs. 6j and 7j). Most of the cavities observed in this study ranged from 50 to 100 μm in size. No cavities smaller than 50 μm were considered in the analysis. Following the removal of the load, the samples were stored at room temperature for a period of 3 months to facilitate healing of the cavities. Subsequently, a scan is conducted, revealing the results in the seventh step (Figs. 6g and 7g). During the eighth stage, a minimal load of 10 N is applied to both samples, and further analysis is conducted. Here it can be mentioned that this minimal load does not generate new cavities, but it might influence the existing residual stresses, leading to a redistribution of stress within the sample area. This redistribution may enhance the visibility or detectability of preexisting microcavities under X-ray microtomography

(Figs. 6h and 7h). The four largest cavities in both cases are comparable, with the highest cavity diameter measuring 0.60 mm in 1-butylimidazole-treated BIIR and 0.64 mm in sulfur-cured BIIR (Figs. 6k and 7k). In terms of numerical aspect, 1-butylimidazole-treated BIIR initially had more cavities, but only 165 cavities remained after healing. In contrast, sulfur-cured BIIR had a total of 234 cavities after this step (Figs. 6l and 7l). The data reveals that sulfur-cured BIIR experienced a reduction of 18 % cavities, whereas 1-butylimidazole-treated BIIR exhibited a substantial reduction of 72 % cavities during the healing process. The closing or the disappearance of cavities can also be seen from the two-dimensional images in case of 1-butylimidazole-treated BIIR (red circles, from Fig. 7f to h). In contrast, minimal changes in cavity sizes can be noticed in sulfur-cured BIIR (red circles, from Fig. 6f to h). In the 1-butylimidazole-treated BIIR, compression marks observed around the cavities indicating complex relaxation behavior of the material towards closing the cavities. This process likely involves the closure of small microcracks around the cavities, which contributes to the reduction in the size of larger cavities. These marks could be the visual manifestation of the molecular level ionic rearrangement of the imidazolium bromide groups. In the case of reversible network consisting elastomer systems, long time relaxation mechanisms (supporting information Figure S5c and S5d) are somewhat different to covalent crosslinked polymer networks and can be described by different theoretical approaches [42–44]. In Ref. [42], the role of weakly associating reversible cross-linkers on the diffusion of a primitive chain through slip-links was considered and the evolution of the entangled chains, as influenced by tethered reversible linkers, was estimated. By approximating the slowing down effect of the associated groups, on the chain motion, as an effective friction, the contribution of the associating groups to the relaxation modulus could be calculated.

4. Conclusion

This work introduces a dual dynamic reversible interaction within the BIIR network structure, achieved by incorporating 1-butylimidazole and a special type of carbon black with a very high surface area, which manifests reversible network along with cation-π and π-π interactions occurring simultaneously in the elastomer. The cation-π interaction facilitated excellent dispersion and strong interaction between the graphitic layers of carbon black and the ionically treated elastomer matrix as supported by Payne effect measurements resulting in excellent mechanical properties in the composite, achieving ca. 14 MPa tensile strength and ca. 1000 % elongation at break. Furthermore, the synergistic effect of both the interactions lead to significantly lower crack growth in the stable crack growth region of crack growth vs tearing energy plot in ionically treated BIIR compared to its sulfur-cured counterpart. X-ray microtomography studies also showed that 72 % of the microcavities formed in ionically treated BIIR healed effectively over time, significantly improving the durability of the material. This result perfectly aligns with results from conventional self-healing experiments, where a 71 % self-healing efficiency in terms of elongation at break was observed. The high mechanical properties and reversible characteristics of ionically treated BIIR present a promising sustainable alternative for real-world applications, such as inner-liners of tires. Moreover, X-ray microtomography could be efficiently utilized to examine the healing process of microcavities, providing a valuable tool for characterizing macro-scale reversibility in various dynamically crosslinked elastomeric materials.

CRediT authorship contribution statement

Subhradeep Mandal: Writing – original draft, Investigation, Formal analysis, Conceptualization. **Arpita Kundu:** Writing – review & editing, Investigation, Formal analysis. **Eric Euchler:** Writing – review & editing, Methodology, Investigation. **Radek Stoček:** Writing – review & editing, Methodology, Investigation. **Ricardo Bernhardt:** Writing – review & editing, Methodology, Investigation. **Peter Reinig:** Writing – review & editing, Methodology, Investigation. **Muhannad Al Aiti:** Writing – review & editing, Methodology, Investigation. **Jun Sawada:** Writing – review & editing, Formal analysis. **Toshio Tada:** Writing – review & editing, Project administration, Conceptualization. **Gianaurelio Cuniberti:** Writing – review & editing, Formal analysis. **Gert Heinrich:** Writing – review & editing, Project administration, Conceptualization. **Sven Wießner:** Writing – review & editing, Supervision, Resources, Project administration, Conceptualization. **Amit Das:** Writing – review & editing, Supervision, Resources, Project administration, Formal analysis, Conceptualization.

Declaration of competing interest

The authors declare that they have no known competing financial interests or personal relationships that could have appeared to influence the work reported in this paper.

Acknowledgement

S.M. and S.W acknowledges “ModEl-FuturE” project carried out under the M-ERA.NET 3 scheme (European Union’s Horizon 2020 research and innovation programme) under grant agreement No 958174. A.D. and S.M acknowledge Deutsche Forschungsgemeinschaft (DFG; German Research Foundation) project 404941515 under SPP2100 Programme for partial financial support. G.H. acknowledges the DFG (Deutsche Forschungsgemeinschaft) research training group“-Interactive Fiber-Rubber Composites” Project 380321452/GRK2430. The Raman work of P. Reinig is partly funded by the Federal Ministry of Education and Research (BMBF) under the project reference numbers 16FMD01K, 16FMD02 and 16FMD03.

Appendix A. Supplementary data

Supplementary data to this article can be found online at https://doi.org/10.1016/j.polymer.2025.128690.

Data availability

Data will be made available on request.

References

[1] M. Costamagna, V. Brunella, M.P. Luda, U. Romagnolli, B. Muscato, M. Girotto, M. Baricco, P. Rizzi, Environmental assessment of rubber recycling through an innovative thermo-mechanical devulcanization process using a Co-rotating twin-screw extruder, J. Clean. Prod. 348 (2022) 131352.
[2] J.I. Gumede, B.G. Hlangothi, C.D. Woolard, S.P. Hlangothi, Organic chemical devulcanization of rubber vulcanizates in supercritical carbon dioxide and associated less eco-unfriendly approaches: a review, Waste Manag. Res. 40 (5) (2022) 490–503.
[3] R. Ghosh, C. Mani, R. Krafczyk, R. Schnell, A. Paasche, A. Talma, A. Blume, W. K. Dierkes, New route of tire rubber devulcanization using silanes, Polymers 15 (13) (2023) 2848.
[4] W. Wang, K. Hao, X. Guo, F. Liu, Y. Xu, S. Guo, L. Bai, G. Liu, L. Qu, M. Liu, Mechano-chemical rubber reclamation using aminolysis products of waste flexible polyurethane foams as the devulcanizing agent, J. Clean. Prod. 384 (2023) 135421.
[5] S. Ghorai, D. Mondal, S. Hait, A.K. Ghosh, S. Wiessner, A. Das, D. De, Devulcanization of waste rubber and generation of active sites for silica reinforcement, ACS Omega 4 (18) (2019) 17623–17633.
[6] M. Vahdatbin, M. Jamshidi, Using chemical agent in microwave assisted devulcanization of NR/SBR blends: an effective recycling method, Resour. Conserv. Recycl. 179 (2022) 106045.
[7] M. Shabani, M. Jamshidi, Recycling NR/SBR waste using probe sonication as a new devulcanizing method; study on influencing parameters, RSC Adv. 12 (40) (2022) 26264–26276.
[8] S. Mandal, A. Das, E. Euchler, S. Wiessner, G. Heinrich, J. Sawada, R. Matsui, T. Nagase, T. Tada, Dynamic reversible networks and development of self-healing rubbers: a critical review, Rubber Chem. Technol. 96 (2) (2023) 175–195.
[9] S. Mandal, I. Arief, S. Chae, M. Tahir, T.X. Hoang, G. Heinrich, S. Wießner, A. Das, Self-repairable hybrid piezoresistive-triboelectric sensor cum nanogenerator utilizing dual-dynamic reversible network in mechanically robust modified natural rubber, Adv. Sens. Res. (2024) 2400036.

[10] L. Kong, Y. Yang, M. Wu, X. Teng, Y. Wang, C. Xu, Design of epoxidized natural rubber/poly (lipoic acid) elastomer with fast and efficient self-healing under a mild temperature, Int. J. Biol. Macromol. 223 (2022) 446–457.
[11] B.N. Yeşil, T. Ünügül, B. Karaağaç, Self-healing behaviour of lignin-containing epoxidized natural rubber compounds, Express Polym. Lett. 17 (7) (2023) 704–721.
[12] W. Liu, J. Huang, Z. Gong, J. Fan, Y. Chen, Healable, recyclable and mechanically robust elastomers with multiple dynamic cross-linking bonds, Polymer 252 (2022) 124900.
[13] L. Huang, Y. Yang, Z. Niu, R. Wu, W. Fan, Q. Dai, J. He, C. Bai, Boronic ester bonds crosslinked vitrimer elastomers with mechanical robustness, shape memory, self-healing and recyclability properties, Compos. Sci. Technol. 228 (2022) 109621.
[14] P. Wu, L. Liu, Z. Wu, A transesterification-based epoxy vitrimer synthesis enabled high crack self-healing efficiency to fibrous composites, Compos. Appl. Sci. Manuf. 162 (2022) 107170.
[15] S. Mandal, F. Simon, S.S. Banerjee, L.B. Tunnicliffe, C. Nakason, C. Das, M. Das, K. Naskar, S. Wiessner, G. Heinrich, Controlled release of metal ion cross-linkers and development of self-healable epoxidized natural rubber, ACS Appl. Polym. Mater. 3 (2) (2021) 1190–1202.
[16] S.W. Wajge, D. Basu, A. Das, S. Mandal, P.K. Maji, S. Singh, C. Das, Dynamic co-ordination networks in carboxylated nitrile rubber and development of self-healing and recyclable rubber composites, J. Polym. Sci. 62 (10) (2024) 2103–2115.
[17] S. Mandal, S. Hait, F. Simon, A. Ghosh, U. Scheler, I. Arief, T. Tada, T.X. Hoang, S. Wießner, G. Heinrich, Transformation of epoxidized natural rubber into ionomers by grafting of 1 H-Imidazolium ion and development of a dynamic reversible network, ACS Appl. Polym. Mater. 4 (9) (2022) 6612–6622.
[18] J. Sawada, S. Mandal, A. Das, G. Heinrich, T. Tada, Hydrogen bonding network formation in epoxidized natural rubber, Polym. Bull. 81 (7) (2024) 5991–6002.
[19] A. Das, A. Sallat, F. Böhme, M. Suckow, D. Basu, S. Wießner, K.W. Stöckelhuber, B. Voit, G. Heinrich, Ionic modification turns commercial rubber into a self-healing material, ACS Appl. Mater. Interfaces 7 (37) (2015) 20623–20630.
[20] S. Mandal, M. Malanin, B. Ghanti, S. Banerjee, J. Sawada, T. Tada, G. Heinrich, S. Wießner, A. Das, Design of sacrificial network in modified natural rubber leads to strikingly improved mechanical performance with self-healing capability, Chem. Eng. J. 474 (2023) 145838.
[21] S. Mandal, O. Verners, E. Euchler, A. Kundu, C. Zimmerer, R. Bernhardt, T. Tada, G. Heinrich, S. Wießner, A. Das, Ionic adaptive network: a sustainable route to replace synthetic rubbers with natural polymers for high-temperature applications, Sustain. Mater. Technol. (2025) e01243.
[22] W. Zhang, B. Wu, S. Sun, P. Wu, Skin-like mechanoresponsive self-healing ionic elastomer from supramolecular zwitterionic network, Nat. Commun. 12 (1) (2021) 4082.
[23] M.W. Urban, D. Davydovich, Y. Yang, T. Demir, Y. Zhang, L. Casabianca, Key-and-lock commodity self-healing copolymers, Science 362 (6411) (2018) 220–225.
[24] G. Kraus, Reinforcement of elastomers by carbon Black, Rubber Chem. Technol. 51 (2) (1978) 297–321.
[25] S.C. Ambilkar, B.P. Kapgate, A. Das, S. Mandal, P.K. Maji, S. Singh, R. Kasilingam, R.S. Gedam, C. Das, Precise role of zirconia to boost up the mechanical, thermal, viscoelastic, dielectric, and chemical resistance properties of natural rubber-nitrile rubber blend, Eur. Polym. J. 194 (2023) 112163.
[26] E. Euchler, R. Bernhardt, K. Schneider, G. Heinrich, S. Wießner, T. Tada, In situ dilatometry and X-Ray microtomography study on the formation and growth of cavities in unfilled styrene-butadiene-rubber vulcanizates subjected to constrained tensile deformation, Polymer 187 (2020) 122086.
[27] R. Stoček, Some revisions of fatigue crack growth characteristics of rubber. Fatigue Crack Growth in Rubber Materials: Experiments and Modelling, 2021, pp. 1–18.
[28] G. Heinrich, R. Kipscholl, R. Stoček, Fatigue crack growth in rubber materials, Adv. Polym. Sci. (2021).
[29] G. Lake, P. Lindley, The mechanical fatigue limit for rubber, J. Appl. Polym. Sci. 9 (4) (1965) 1233–1251.
[30] O. Peter, M. Stěnička, G. Heinrich, C.G. Robertson, J. Pawlas, R. Stoček, J. Ondrík, The tearing energy threshold of crack growth in rubber exposed to ozone: an experimental–numerical approach, Int. J. Fract. (2024) 1–18.
[31] G. Lake, O. Yeoh, Measurement of rubber cutting resistance in the absence of friction, Int. J. Fract. 14 (1978) 509–526.
[32] C.G. Robertson, R. Stoček, W.V. Mars, The fatigue threshold of rubber and its characterization using the cutting method. Fatigue Crack Growth in Rubber Materials: Experiments and Modelling, 2021, pp. 57–83.
[33] L. Cançado, K. Takai, T. Enoki, M. Endo, Y. Kim, H. Mizusaki, A. Jorio, L. Coelho, R. Magalhães-Paniago, M. Pimenta, General equation for the determination of the crystallite size La of nanographite by Raman spectroscopy, Appl. Phys. Lett. 88 (16) (2006).
[34] V. Bušić, D. Gašo-Sokač, Menshutkin reaction in choline chloride-based deep eutectic solvents, Org. Prep. Proced. Int. 55 (2) (2023) 160–166.
[35] K. Chumnum, E. Kalkornsurapranee, J. Johns, K. Sengloyluan, Y. Nakaramontri, Combination of self-healing butyl rubber and natural rubber composites for improving the stability, Polymers 13 (3) (2021) 443.
[36] D. Pantea, H. Darmstadt, S. Kaliaguine, C. Roy, Electrical conductivity of conductive carbon blacks: influence of surface chemistry and topology, Appl. Surf. Sci. 217 (1–4) (2003) 181–193.
[37] J. Wu, G. Huang, Q. Pan, J. Zheng, Y. Zhu, B. Wang, An investigation on the molecular mobility through the glass transition of chlorinated butyl rubber, Polymer 48 (26) (2007) 7653–7659.
[38] J. Liu, C. Xiao, J. Tang, Y. Liu, J. Hua, Construction of a dual ionic network in natural rubber with high self-healing efficiency through anionic mechanism, Ind. Eng. Chem. Res. 59 (28) (2020) 12755–12765.
[39] D. Basu, A. Das, K.W. Stöckelhuber, D. Jehnichen, P. Formanek, E. Sarlin, J. Vuorinen, G. Heinrich, Evidence for an in situ developed polymer phase in ionic elastomers, Macromolecules 47 (10) (2014) 3436–3450.
[40] G. Kraus, Mechanical losses in carbon-black-filled rubbers. Applied Polymer Symposium, Journal of Applied Polymer Science, 1984, pp. 75–92.
[41] A. Kundu, I. Arief, S. Mandal, K.K. Meena, B. Krause, U. Staudinger, T. Mondal, S. Wießner, A. Das, Elastomeric sensor-triboelectric nanogenerator coupled system for multimodal strain sensing and organic vapor detection, ACS Appl. Mater. Interfaces (2024).
[42] M.J. Mateyisi, J.-U. Sommer, K.K. Müller-Nedebock, G. Heinrich, Influence of weak reversible cross-linkers on entangled polymer melt dynamics, J. Chem. Phys. 148 (24) (2018).
[43] M. Rubinstein, R.H. Colby, Polymer Physics, Oxford University Press, 2003.
[44] G. Heinrich, T. Vilgis, Long-time relaxation of polymer networks, Macromolecules 25 (1) (1992) 404–407. TOC.